Jpn. J. Appl. Phys. Vol. 42 (2003) pp. 375–383
Part 1, No. 2A, February 2003
©2003 The Japan Society of Applied Physics

Band Gap Reduction in InAsN Alloys

Ding-Kang SHIH[1], Hao-Hsiung LIN[1*], Li-Wei SUNG[1], Tso-Yu CHU[1] and T.-R. YANG[2]

Department of Electrical Engineering, National Taiwan University, Taipei, Taiwan, R.O.C.
[1]*Graduate Institute of Electronics Engineering, National Taiwan University, Taipei, Taiwan, R.O.C.*
[2]*Department of Physics, National Taiwan Normal University, Taipei, Taiwan, R.O.C.*

(Received May 7, 2002; revised manuscript received September 9, 2002; accepted for publication September 17, 2002)

We report the structural, electrical and optical properties of bulk InAsN alloy with various nitrogen contents deposited on (100) InP substrates using plasma-assisted gas-source molecular beam epitaxy. From absorption measurements, it is found that the fundamental absorption energy of InAsN is higher than that of InAs due to the Burstein–Moss effect resulting from the high residual carrier concentration in InAsN. To deduce the 'real' band-gap energy of InAsN samples, the energy shift due to the Burstein–Moss effect and the band-gap narrowing effect are calculated by using a self-consistent approach based on the band-anticrossing (BAC) model [Shan *et al.*: Phys. Rev. Lett. **82** (1999) 1221]. After correction, the 'real' band-gap energy of InAsN samples decreases as N increases. The electron effective mass of InAsN is also investigated by plasma-edge measurement. We found a sizeable increase of the electron effective mass in these InAsN alloys, which is consistent with the theoretical predictions based on the BAC model. [DOI: 10.1143/JJAP.42.375]

KEYWORDS: InAsN, gas source MBE, nitride, Burstein–Moss effect, localized state, infrared reflectivity, effective mass

1. Introduction

Low-nitrogen-content zincblende III–V alloys have received much attention in the past few years.[1–3] The large difference in atomic size and electronegativity between N and As has motivated the development of many theoretical approaches to understand the huge bowing parameter, and to ascertain the semiconducting or semimetallic nature of these alloys.[4–6] Over the last few years, there have been numerous attempts to explain the large band-gap reduction properties of III–V–N alloys.[7–10] It has been demonstrated recently that a band anticrossing (BAC) model in which localized N states interact with the extended states of the conduction band can explain the unusual properties of III–V–N alloys.[10,11]

The diluted III–V–N alloys are also very promising for long-wavelength optoelectronic device and high-efficiency hybrid solar cell applications. In the mid-infrared 2–5 μm wavelength region, the InAsN alloy may be a very promising material. In a previous study, we demonstrated a high-quality 2.2 μm InAs/InGaAs/InP highly strained multiple quantum well (MQW) laser grown by gas-source molecular-beam epitaxy (GSMBE).[12] Using InAsN to replace InAs can alleviate the critical thickness limitation of the quantum well because of its small lattice constant. In addition, the band-gap energy of the quantum well can also be reduced further because of the huge bowing effect. These two features reveal the possibilities of extending the wavelength of lasers on InP substrates to the longer infrared range. The first $InAs_{0.97}N_{0.03}$/InGaAs/InP quantum well laser lasing at 2.38 μm under pulse operation at 260 K, which was grown by GSMBE, has recently been reported.[13] Although the InAsN laser has been already demonstrated, unlike the extensively studied InGaAsN, GaAsN and other III–V–N compounds, there are still substantial physical properties that remain to be elucidated for the InAsN alloy. In this study, we have investigated a series of unintentionally doped InAsN bulk layers with various N contents grown on InP substrates using GSMBE. We found that these samples have high residual carrier concentration that increases as N content increases. Furthermore, the fundamental absorption edge of InAsN, compared to that of InAs, shifts to higher energies due to the Burstein–Moss (BM) effect.[14] To deduce the 'real' band-gap energy of InAsN samples, the energy shift due to the BM effect and the band-gap narrowing (BGN) effect is considered using a self-consistent approach based on the BAC model. After the correction, the 'real' band-gap energy of InAsN samples decreases as N increases, and obeys the bowing effect. In addition, we found a dramatic increase of the electron effective mass in these InAsN alloys, which is consistent with the theoretical predictions based on the BAC model.

2. Experiments

The samples were grown on semi-insulating (100) InP substrates using a VG V-80H GSMBE system. Elemental In source and thermally cracked AsH_3 and PH_3 sources were used. The active N species were generated from an EPI UNI-bulb RF plasma source. The RF power and nitrogen flow rate used for these growths ranged from 300 W to 480 W and from 0.5 to 1.9 sccm, respectively. Detailed growth conditions are summarized in Table I and described elsewhere.[15] To start the growth, the InP substrate was desorbed at 500°C under P_2 flux. Then, a 0.3-μm-thick undoped InP buffer layer was deposited at 460°C at a rate of 1.5 μm/h. A 2-μm-thick undoped InAs(N) was subsequently overgrown on the buffer

Table I. Growth conditions and nitrogen composition of InAsN on InP substrate.

Sample no.	RF plasma power (W)	Flow rate of N_2 (sccm)	Nitrogen composition (%)
C937	0	0	0
C1076	300	1.2	0.5
C1077	400	1.2	1.6
C1078	480	1.2	2.8
C1117	300	1.9	0.8
C1118	300	1.5	1.2
C1129	480	0.5	0.1
C1130	480	0.9	0.5
C1132	480	1.8	2.8

*Corresponding author. E-mail address: hhlin@cc.ee.ntu.edu.tw

layer without growth interruption and the AsH_3 flow rate was fixed at 4 sccm. High-brightness mode N_2 plasma was ignited for the N-containing growth. The RF power was turned off immediately after finishing the InAsN growth. Besides the InAsN sample, a controlled InAs sample was also grown. Their growth conditions were kept the same except the irradiation of active N species.

The structural properties of the InAsN layers were characterized using a Bede D3 high-resolution X-ray diffractometer (HRXRD), a Bede QC1a X-ray double crystal X-ray diffractometer (DXRD), an SPM Solver P47 atomic force microscope (AFM), and a CAMECA IMS-5F secondary-ion-mass spectroscope (SIMS). All the XRD spectra in this study were measured in the $\theta/2\theta$ mode. AFM measurements were carried out in ambient environment with a scan size of $4\,\mu m \times 4\,\mu m$. The electrical properties of the samples were investigated by Hall-effect measurements. The Van der Pauw geometry with soldered indium dots as ohmic contacts was used. Infrared reflectivity and transmission measurements were performed at room temperature using a Bruker IFS 120 HR Fourier-transform infrared (FTIR) spectrometer.

3. Results and Analysis

Since phase separation has been reported in III–V–N alloys, the structural properties of these InAsN films were studied first. Figure 1 is a typical (004) HRXRD scan profile of an InAsN sample (C1077). From the figure, we can see that there are no X-ray peaks associated with cubic InAs, cubic InN, or hexagonal InN, which indicates no phase separation (namely poly-phase) in the InAsN film and confirms the formation of a single InAsN crystal in this study. Figure 2 shows the (004) DXRD rocking curves of InAs and InAsN samples. Upon increasing the plasma power or the N_2 flow rate, the diffraction peak of the InAsN, compared with that of InAs sample, shifts toward the InP substrate peak, demonstrating the reduction of the lattice constant due to N incorporation. The alloy compositions of the InAsN layers were determined from the DXRD spectra fittings using a commercially available dynamic simulator, RADS. The N compositions determined from RADS fitting are summarized in Table I. Since the film thickness is much larger than the critical layer thickness calculated from Matthews and Blakeslee's model[16] (4 nm and in some nonequilibrium growth conditions it might be two times larger) and the thermal expansion coefficient of InAs is very close to that of InP,[17] the InAsN samples are assumed to be fully relaxed. Although N was successfully incorporated into InAs, its incorporation significantly degrades the DXRD linewidths as compared to the reference InAs sample. In order to examine the N content in the InAsN crystal, SIMS depth measurement was performed. Figure 3 shows an in-depth SIMS profile. The In, As, N, P and O signals were analyzed. It can be seen that a clear nitrogen signal was detected in the InAsN layer and there is no detectable P in

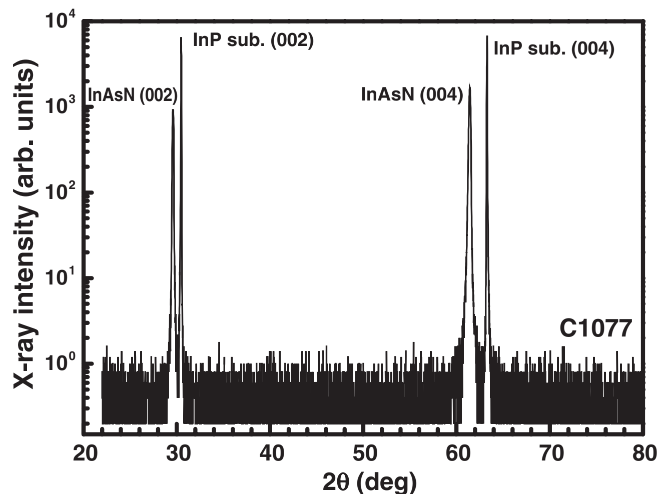

Fig. 1. Typical X-ray θ–2θ scan profile of an InAsN sample (C1077), showing no phase separation.

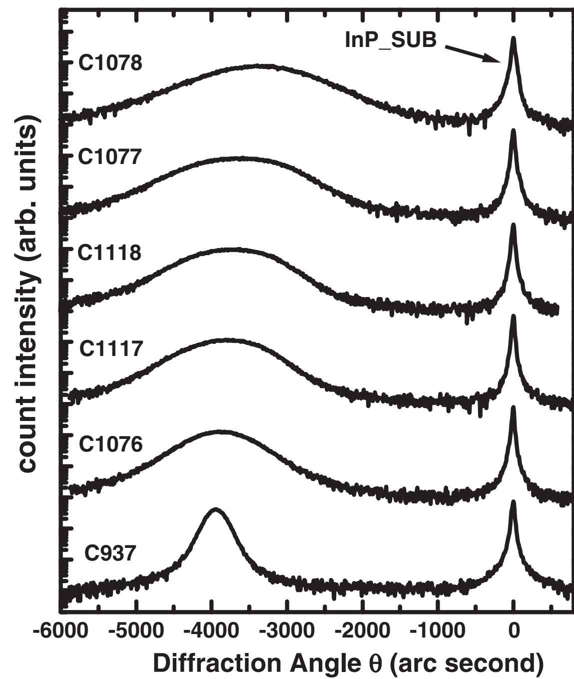

Fig. 2. DXRD spectra of a series of $InAs_{1-x}N_x$ bulk samples with x ranging from 0 to 0.028.

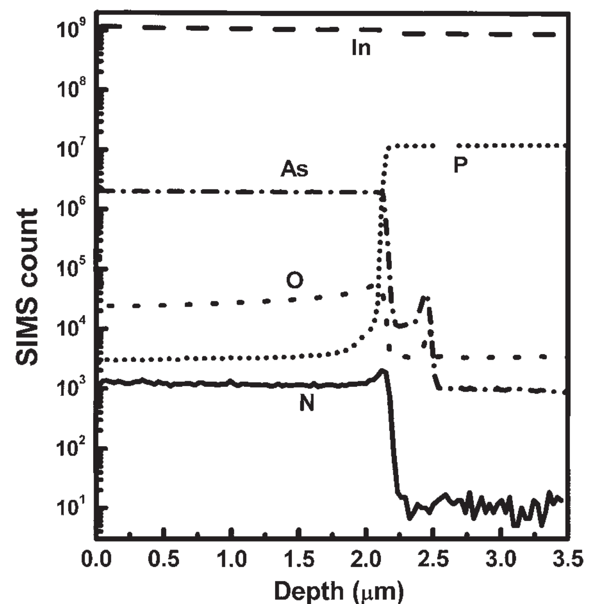

Fig. 3. Depth profile of InAsN sample analyzed by SIMS.

Table II. Room-temperature Hall mobility and residual carrier concentration of the InAsN samples.

Sample no.	N (%)	Residual carrier conc. n_D (cm^{-3})	Mobility (cm^2/Vs)
C937	0	2.64×10^{16}	7660
C1129	0.1	9.87×10^{17}	3530
C1130	0.5	1.69×10^{18}	2140
C1076	0.5	1.91×10^{18}	1740
C1117	0.8	1.21×10^{18}	2690
C1118	1.2	8.85×10^{17}	3290
C1077	1.6	3.24×10^{18}	1280
C1132	2.8	2.80×10^{18}	1010
C1078	2.8	1.69×10^{19}	38.1

the InAsN epilayer.

Table II shows the Hall results of the samples at room temperature. All the intentionally undoped samples exhibit n-type conduction, and the larger the N content, the higher the carrier concentration. The origin of the high background n-type doping in N-containing sample is still under investigation. However, because of the large InAs crystal lattice constant and the small N atom size, nitrogen interstitial defects could be a possible candidate. Furthermore, since the band gap is very narrow, the defect levels in these materials could be ionized to result in high residual carrier concentration. In these samples, the electron mobility drops from 7.66×10^3 cm^2/Vs in the reference InAs sample to 38.1 cm^2/Vs in sample C1078 ($x = 0.028$ with a residual carrier concentration of 1.69×10^{19} cm^{-3}). This phenomenon can be attributed to the nitrogen incorporation into the alloy. As mentioned above, the incorporation drastically deteriorates the material quality, which may introduce scattering centers for residual carriers. In addition, the increase of electron effective mass due to the nitrogen incorporation should also be taken into account. According to the BAC model, the dispersion relation of the nonparabolic subbands becomes flatter as the nitrogen content is increased. This indicates a large increase of the effective mass in the subbands.[18,19] Among these N-containing samples, C1078 has the highest residual free carrier concentration and an extraordinarily low mobility. The very high residual free carrier concentration in C1078 may make the nonparabolic effect on the subband much more significant, and therefore results in very low mobility. Similar results have been reported by Skierbiszewski *et al.*[19]

The surface roughness was determined by tapping-mode AFM using SiN tips. The AFM images of these InAsN films indicate that the root mean square (rms) surface roughness is between 3 and 14 nm, depending on the nitrogen compositions of the samples. In fact, as plasma power increased (indicating more N was generated and incorporated into the InAs), the reflection high-energy electron diffraction (RHEED) pattern observed during the growth became spottier and dimmer, indicating a three-dimensional growth mode. Figure 4 shows the relationship between the rms surface roughness and mobility. N content of each sample is also indicated in the figure. As indicated in the figure, the mobility decreases as N content increases. Surface roughness scattering has a significant influence on the mobility only when the layer thickness is comparable to the surface roughness, such as in the case of silicon inversion layers. In this study, the rms surface roughness of InAsN films is between 3 and 14 nm and the film is 2 μm thick, which is much larger than the rms surface roughness. Therefore, the effect of surface roughness scattering on electron transport could be neglected.

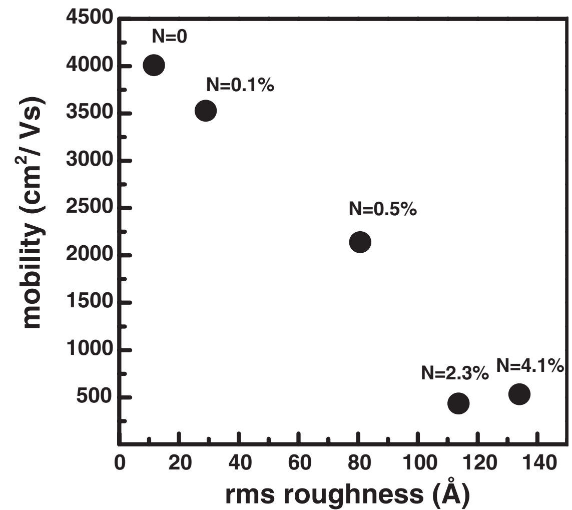

Fig. 4. Relationship between rms surface roughness and mobility. N content of each sample is also indicated in the figure.

Figure 5 shows the near band edge absorption spectra at room temperature. The absorption coefficient α is obtained from FTIR transmission measurements. Two points are worth noting from this figure. First, the energy of the absorption edge of InAsN samples is always higher than that of InAs. Second, when the N content is lower than 1.6%, a higher N content leads to a higher absorption edge. However, the trend reverses for InAsN with higher N content. The phenomenon seems to contradict the theoretical prediction. To interpret the results, the BM effect should be taken into account owing to the high residual carrier concentration in these InAsN samples. Samples with lower N concentration have smaller effective mass and thus display more BM shift. The two high N content samples, however, have larger effective mass and thus their BM effects are less

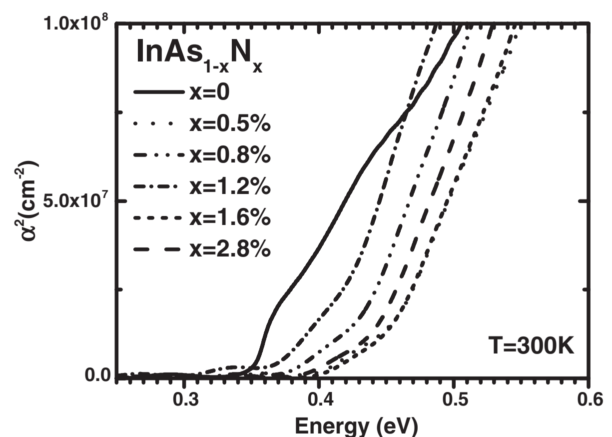

Fig. 5. Plots of the square of the absorption coefficient (α^2) vs the photon energy deduced from 300 K IR transmission spectra recorded on a series of $InAs_{1-x}N_x$.

significant. In these two samples, C1078 (2.8%) and C1077 (1.6%), the bowing effect on the band-gap may have overcome the BM effect, resulting in the red-shifted absorption edge, although the carrier concentration of the former is five times higher than that of the latter.

To deduce the 'real' band-gap energy of our InAsN samples, the energy shift due to the BM effect and the BGN, which is always accompanied by the BM effect, are considered using a self-consistent approach based on the BAC model. According to the BAC model, the interaction of the conduction band edge with the highly localized N states leads to a splitting of the conduction band into two highly nonparabolic subbands E_- and E_+ with dispersion relations given by

$$E_{\pm}(k) = \frac{1}{2}\left\{[E_M(k) + E_N] \pm \sqrt{[E_M(k) - E_N]^2 + 4V_{NM}^2}\right\}, \quad (1)$$

where E_N is the energy of the nitrogen state, $E_M(k)$ is the dispersion relation for the conduction band of the N-free semiconductor matrix, and V_{NM} is the matrix element coupling those two types of states. All energies are measured relative to the top of the valence band. The downward shift of the lower subband E_- can account well for the reduction of the fundamental band gap observed in these III–V–N alloys.

It is evident from eq. (1) that the initial rate of the N-induced band gap reduction depends on the coupling parameter V_{NM} and on the energy difference $E_M - E_N$. Therefore, the dependence of E_N, E_M, and V_{NM} on the nitrogen content of the InAsN bulk layer should be duly taken into account. In the case of InAsN, we determined the E_N based on the following assumptions: The existing experimental results on the location of E_N in different III–V group materials indicate that, similar to many other highly localized centers, the energy of the nitrogen level is constant relative to the common energy reference or vacuum level.[20,21] Using the known conduction band offset we can determine E_N in InAs. It is well known that in GaAs, E_N lies at about 0.23 eV above the conduction band edge. Therefore, the energy of the highly localized nitrogen level ($E_N = 1.48$ eV) relative to top of the valence band maximum in InAs was estimated from the valence band offset, ΔE_V (GaAs/InAs) $= 0.17$ eV.[22] Concerning the dispersion relation $E_M(k)$ for the conduction band of InAs, we adopted the calculated results of ref. 23, which are based on the triple-band effective-mass approximation, and $E_M(0) = 0.35$ eV at room temperature. For V_{NM}, it has been shown previously that the square of the matrix elements is proportional to the concentration of nitrogen atoms, i.e., $V_{NM} = C_{NM}x^{1/2}$, where C_{NM} is a constant that depends on the semiconductor matrix[10,24] and is treated as a fitting parameter in this study.

In the present case, according to the schematic band structure of InAsN shown in Fig. 6, the absorption edge E_{abs} is

$$E_{abs} = E_- + E_{BM} - E_{BGN}, \quad (2)$$

where E_{BM} is the energy shift due to the Burstein–Moss effect, and E_{BGN} is the reduction energy due to the band-gap narrowing effect. To estimate E_{BM}, we solve the Fermi energy E_F in the conduction band from the following equation,

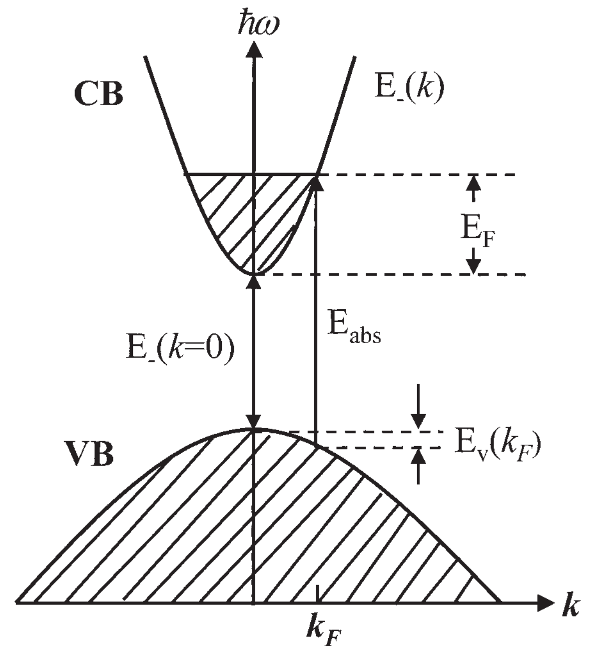

Fig. 6. Schematic of the band structure of a heavily doped n-type InAsN. The conduction band (CB) and the valence band (VB) were assumed to be parabolic. Shaded areas denote the regions occupied by electrons.

$$n_D = \int f(E_-)D(E_-)dE_-, \quad (3)$$

where n_D is the residual carrier concentration from the Hall measurements, $f(E_-)$ is the Fermi–Dirac distribution, and $D(E_-)$ is the density-of-states function in the lower subband conduction band, E_-. The BM shift in the valence band is

$$E_V(k_F) = \frac{\hbar^2 k_F^2}{2m_h^*}, \quad (4)$$

where k_F is the Fermi wave number and is given by $k_F = (3\pi^2 n_D)^{1/3}$, m_h^* is the effective mass of the heavy-hole (assuming that heavy-hole valence band is parabolic), and $\hbar$ is Planck's constant. Using photomodulation spectroscopy, Shan *et al.* found that the energetic location of the valence band was nearly independent of the nitrogen content in $GaAs_{1-x}N_x$ ($x < 3\%$) alloys.[10,25] Furthermore, the theoretical calculations by Bellaiche *et al.*[26] showed that the valence band discontinuity between $GaP_{1-x}N_x$ and GaP was almost zero within $x < 5\%$. Therefore, we assume that the perturbation induced by N on the valence band can also be omitted in InAsN. The absorption from the light-hole band is neglected because of its very low density of states. In addition, the band-gap narrowing due to band tails is not considered either.[27] Now, the band-gap widening E_{BM} for carrier concentration n_D is expressed as

$$E_{BM} = E_F + E_V(k_F). \quad (5)$$

Concerning the BGN due to the residual carrier, the shrinkage in energy is proportional to the carrier concentration and an empirical relation[28,29] can be represented by

$$E_{BGN} = \alpha_{InAsN} n_D^{\frac{1}{3}}, \quad (6)$$

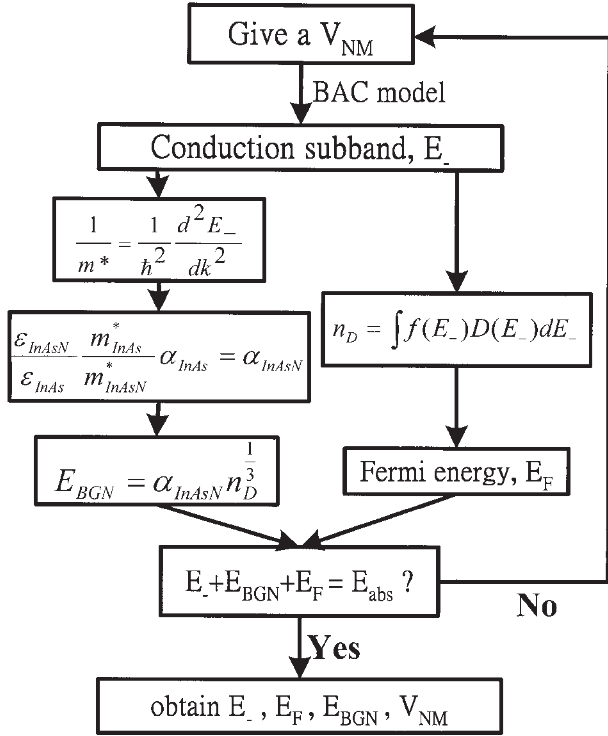

Fig. 7. Block diagram illustrating the procedure that was used in this study to solve the unknown values E_{BM}, E_-, E_{BGN}, and V_{NM}.

where α_{InAsN} is the band-gap narrowing coefficient.

To solve E_- from eq. (2), we adopted the following procedure that is shown in Fig. 7. The parameter V_{NM} is the only fitting parameter. With a given V_{NM}, the lower subband $E_-(k)$ can be calculated using eq. (1). Once $E_-(k)$ is determined, we can calculate the density of states $D(E_-)$ and solve E_F using eq. (3) with measured n_D. E_{BM} is thus found by using eqs. (4) and (5). With the calculated $E_-(k)$, we may also calculate the conduction band effective mass,

$$m^*_{InAsN} = \frac{1}{\hbar^2}\frac{d^2E_-}{dk^2}. \quad (7)$$

The band-gap narrowing coefficient α_{InAsN} can be expressed as[30)]

$$\alpha_{InAsN} = \left[(\varepsilon_{InAsN}/\varepsilon_{InAs})(m^*_{InAs}/m^*_{InAsN})\right]\alpha_{InAs}, \quad (8)$$

where $\varepsilon_{InAs(N)}$ is the static dielectric constant of InAs(N), and we suggest that $\varepsilon_{InAsN} = \varepsilon_{InAs}$ since the nitrogen content is small in the present alloy. For InAs, $m^*_{InAs} = 0.024m_0$, where m_0 is the electron rest mass, and $\varepsilon_{InAs} = 15.15$.[17)] Based on the three effects proposed in ref. 27, the estimated band-gap narrowing energy of InAs increases from ~40 meV to ~100 meV when carrier concentration increases from $n \sim 4 \times 10^{18}\,cm^{-3}$ to $\sim 5 \times 10^{19}\,cm^{-3}$. By using the empirical formula, eq. (6), the BGN coefficient α_{InAs} should be $\sim 2.67 \times 10^{-8}$ meV cm. This value is adopted in this study to estimate α_{InAsN} for the determination of the energy shift caused by the BGN effect, i.e., E_{BGN}. Once the E_-, E_{BM}, and E_{BGN} are determined, E_{abs} can be obtained from eq. (2). If the difference between the calculated E_{abs} and the experimental result is larger than 10^{-4} eV, a new V_{NM} is chosen using the bisection method to calculate a new E_{abs}.

Table III gives the values of E_-, E_{BM}, E_{BGN}, E_F and V_{NM} obtained from the above calculation, along with the residual carrier concentration n_D and absorption edge E_{abs} from the experiments. A plot of V_{NM} versus the square root of nitrogen composition ($x^{1/2}$) is shown in Fig. 8. The solid line is the best fit of $V_{NM} = C_{NM}x^{1/2}$ to the data. The result of the fitting parameter C_{NM}, the coupling parameter in InAs, is 1.68 eV. This value is smaller than those found in InGaAsN with low indium concentration (2.3–2.7 eV),[10,31,32)] and that found in InPN (3.5 eV).[33)] Since the interaction energy V_{NM} is the matrix element coupling the state of the unperturbed conduction band edge at Γ point and a localized state introduced by nitrogen, it is reasonable that the extent of coupling should be weaker in a semiconductor matrix with E_M at Γ point far from the localized E_N level.

Table III. Summary of the computed and experimental energies involved in the self-consistent approach as described in the text. (All energies are given in eV.)

Sample no.	N (%)	E_{abs}	E_F	E_V (k_F)	E_{BM}	E_{BGN}	E_-
C1076	0.5	0.439	0.129	0.010	0.139	0.034	0.334
C1077	1.6	0.439	0.157	0.019	0.176	0.038	0.301
C1078	2.8	0.434	0.255	0.061	0.316	0.061	0.179
C1117	0.8	0.419	0.106	0.010	0.116	0.028	0.331
C1118	1.2	0.406	0.094	0.009	0.103	0.021	0.324
C1129	0.1	0.409	0.094	0.008	0.102	0.026	0.333
C1130	0.5	0.415	0.117	0.012	0.129	0.031	0.317
C1132	2.8	0.423	0.142	0.017	0.159	0.036	0.300

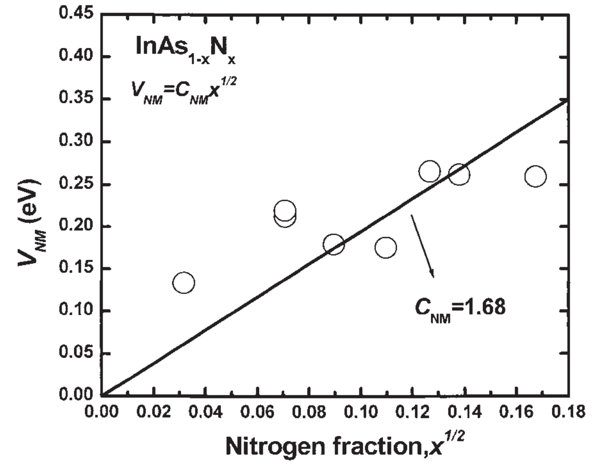

Fig. 8. Dependence of interaction potential, V_{NM}, on nitrogen content for $InAs_{1-x}N_x$. The solid line is the best fit of $V_{NM} = C_{NM}x^{1/2}$ to the data ($C_{NM} = 1.68$ eV).

The dispersion relation of $InAs_{0.97}N_{0.03}$ calculated by the BAC model is shown in Fig. 9 as an example. The parameters used in this calculation [eq. (1)] include the known $E_M(k)$ of InAs, the highly localized nitrogen level $E_N = 1.48$ eV relative to the top of the valence band maximum in InAs, and the best fit value of $C_{NM} = 1.68$. As can be seen in Fig. 9, both E_- and E_+ transitions exhibit a classical anticrossing behavior. Additionally, a distinct flattening of the $E_\pm(k)$ curves for energies approaching E_N is clearly demonstrated, which implies a significant increase of the effective mass of both the subbands as compared to that of InAs.

Deducting the effect of E_{BM} and E_{BGN} on the band gap

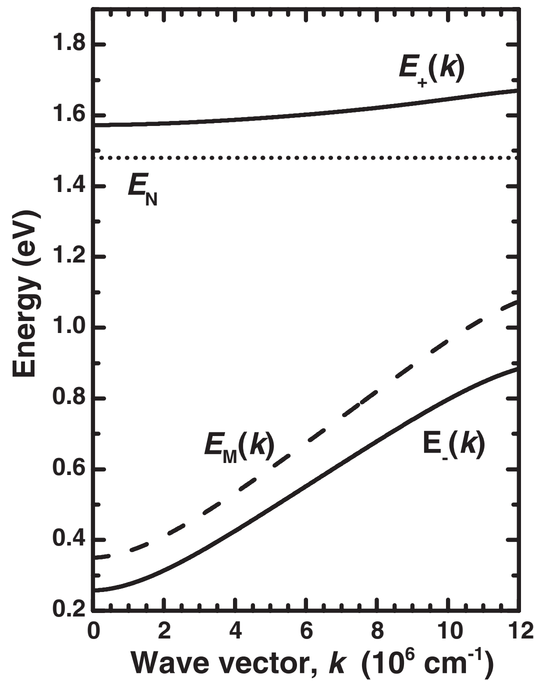

Fig. 9. Calculated dispersion curves for $E_{\pm}$ subbands (solid lines) of the $InAs_{0.97}N_{0.03}$ using the BAC model as described by eq. (1). The dotted lines represent the unperturbed energies of the N level (E_N) and the InAs matrix. It should be noted that a distinct flattening of the $E_{\pm}(k)$ curves for energies approaching E_N is clearly demonstrated.

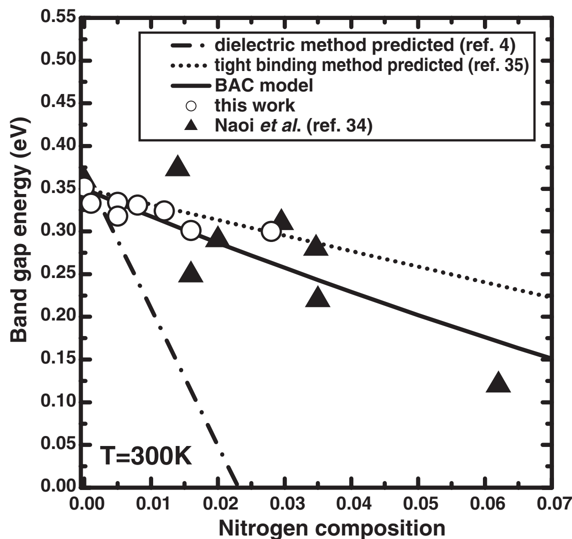

Fig. 10. Composition dependence of the band gap of InAsN. Empty circles represent experimental data, whereas the solid line represents calculated results using the BAC model. Filled triangles are experimental data published in the literature (see ref. 34). Results from dielectric calculations (see ref. 4) and the tight-binding method (see ref. 35) are shown by a dash-dotted line and a dotted line, respectively.

from the absorption peak edge gives the corrected band-gap energy E_- of each InAsN sample. Figure 10 shows the composition dependence of the corrected band-gap energy of InAsN. It is clear that the bowing effect reappears in these samples. Besides our own results, the figure also includes a previously published result from another research group.[34] The three curves represent calculated band gaps based on the BAC model in this study, the dielectric model[4] and the tight binding method.[35] As can be seen, our experimental results are close to the theoretical curve calculated from the BAC model. The estimated transition energy shrinkage coefficient of our bulk InAsN is -15 meV/at.% N. We note that this coefficient is smaller than -31 meV/at.% N in our earlier photoluminescence study on strained $InAs_{1-x}N_x$/InGaAs(P)/InP quantum wells (QWs).[36] The difference due to the strain effect[37,38] is small, about -3 meV/at.% N in this study. Therefore, we considered two other possibilities to interpret this phenomenon. The first is the quantum confinement effect. It is well known in the QW case that the quantum confinement of electrons and holes creates a larger transition energy than that of the bulk, and hence it corresponds to an allowed higher wave number k in the dispersion relations. With a decrease in the width of the well, the quantum levels become higher, and the allowed k values become larger. As mentioned earlier, the interaction between the extended conduction band and the highly localized N states leads to a reduction of the band gap in the III–V–N alloys, and the interaction becomes pronounced as the extended states approach the E_N level. In the InAsN case, E_M $(k = 0)$ is 0.36 eV and the localized nitrogen level $E_N = 1.48$ eV, all relative to top of the valence band maximum. As can be seen in Fig. 11, the position of E_M $(k = 0)$ is far below the E_N state when compared with that of the other III–V–N alloys, such as (In)GaAsN or GaPN alloys. Therefore, less nitrogen-induced perturbation on the Γ band states of InAs is expected. However, in some higher k (QW case) regions for the states located close to E_N, the interaction will be much stronger than that in the lower k region (bulk case). Consequently, the transition energy difference E_W between with and without nitrogen in the QW case is larger than that of E_b in bulk case. These may explain the reason why we

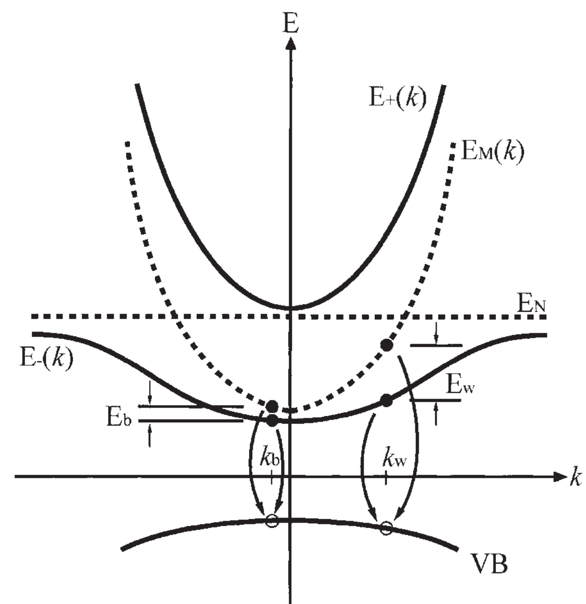

Fig. 11. Schematic of dispersion curves for the lower and upper conduction subbands $E_{\pm}$ in InAsN. The dotted lines represent the unperturbed conduction band of InAs $E_M(k)$ and the nitrogen level E_N. Arrows indicate possible experimental optical transition. As a result of the quantum confinement effect, the allowed wave number k_w in the quantum well case is larger than that of in bulk case, k_b. The transition energy difference E_w between with nitrogen and without nitrogen perturbed in the QW case is obviously larger than the E_b in bulk case.

observed a significant band-gap reduction in the QW structure. The second possibility is the ordering effect. Recently, Bellaiche *et al.* reported the effect of short-[39] and long-range[6] ordering on the band gap of GaAsN. They pointed out that ordered alloys have larger bowing effect than random alloys. This large difference in the bowing coefficient is especially prominent for low nitrogen concentrations. Since the nitrogen concentration in this study is low, the effect may take place in these InAsN alloys. As compared with the previous coherent strained $InAs_{1-x}N_x$/InGaAs(P) QW, all of the samples in this study are fully relaxed, perhaps indicative of a low degree of ordering. A similar phenomenon has also been observed in GaAsN alloys by Francoeur *et al.*[38]

It has been predicted that the nitrogen alloying should increase the electron effective mass of the E_- state. Although a large enhancement of the electron effective mass in InGaAsN and GaAsN as compared to its parental III arsenides without nitrogen, has been recently demonstrated,[18,40] no experimental determination of the InAsN alloy has been reported so far. To verify the effective mass increment predicted by these models, we performed measurements of the infrared reflectivity and Hall effect from which the plasma frequency, ω_p, and the Hall electron concentration, n_D, in these InAsN samples were determined. Typical examples of reflectivity spectra for InAsN samples of different nitrogen compositions and residual carrier concentrations are shown in Fig. 12. As can be seen, the onset of the plasma reflection edge is at $470\,cm^{-1}$ and $617\,cm^{-1}$, respectively. The thin line represents the fitting curve using the method described in ref. 41. The electron effective mass at the Fermi energy can be determined from

$$\omega_p^2 = \frac{N_e(k_F)e^2}{m^*_{exp}(k_F)\varepsilon_\infty\varepsilon_0}, \qquad (9)$$

where e is the electron charge, N_e (k_F) is the free electron concentration, ε_∞ is the high frequency dielectric constant (here we assume an ε_∞ of 12.25[17]), and ε_0 is the permittivity of free space. We also calculated the effective mass using the following equation as described in ref. 23:

$$\omega_p^2 = \int_{E_C}^{\infty} d\omega_p^2(E) = \int_{E_C}^{\infty} \frac{q^2 f(E_-)D(E_-)dE_-}{m_{opt}(E_-)\varepsilon_\infty}, \qquad (10)$$

where m^*_{opt} (E_-) is the optical effective mass defined as $m^*_{opt} = [1/\hbar^2 k(dE_-/dk)]^{-1}$. A detailed definition of the above quantities can be found elsewhere.[42] Substituting plasma wavelength into eq. (9), one can find the electron effective mass. The plasma frequency and the calculated electron effective mass of InAsN samples are summarized in Table IV. As can be seen, a very large increase of the effective mass is found in samples with higher N composition, which is qualitatively in good agreement with the predictions of the BAC model. The electron effective mass of C1078 is extraordinarily larger than those of the other samples. This result supports the arguments we used to interpret the extraordinarily low mobility for the same sample in previous Hall results.

To illustrate the dependence of the effective mass on the electron energy and the nitrogen content, the values of the

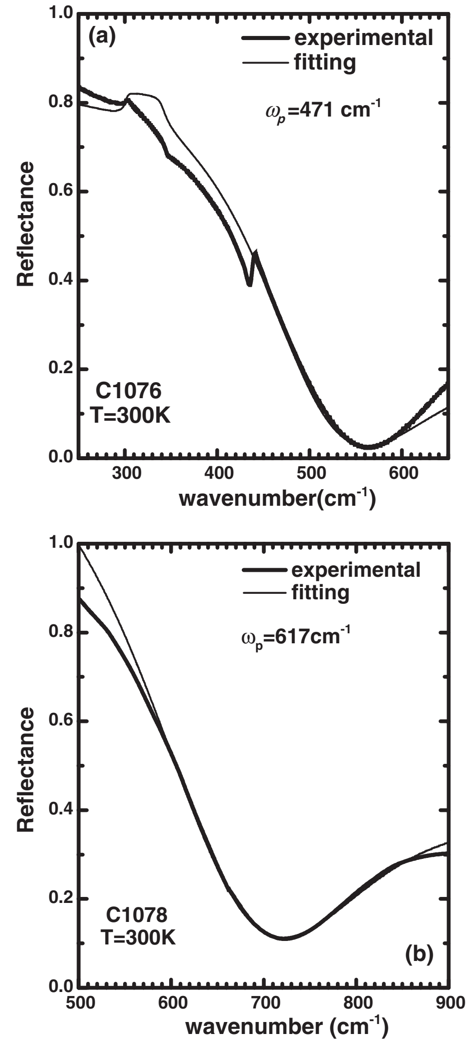

Fig. 12. FTIR-measured plasma reflectance spectra (bold lines) for two samples with different residual carrier concentrations. The thin lines show the best fit using the methods described in ref. 41.

Table IV. Carrier concentration, plasma frequency, and experimental, theoretical calculated electron effective masses of the studied samples.

Sample no.	ω_p (cm^{-1})	Residual carrier concentration n_D (cm^{-3})	m^* (m_0) exp.	m^* (m_0) cal.
C937	—	2.64×10^{16}	—	0.024[a)]
C1076	471	1.91×10^{18}	0.063	0.044
C1077	590	3.24×10^{18}	0.068	0.052
C1078	617	1.69×10^{19}	0.326	0.123
C1117	390	1.21×10^{18}	0.055	0.039
C1118	360	8.85×10^{17}	0.051	0.036
C1129	395	9.87×10^{17}	0.046	0.037
C1130	475	1.69×10^{18}	0.055	0.043
C1132	593	2.80×10^{18}	0.058	0.046

a) ref. 17

experimental effective mass at different electron concentrations are shown in Fig. 13. Solid squares and empty triangles represent experimental data and theoretical values, which span the range of the alloy compositions of the investigated samples. Basically, the experimental results are qualitatively in good agreement with the theoretical results and support

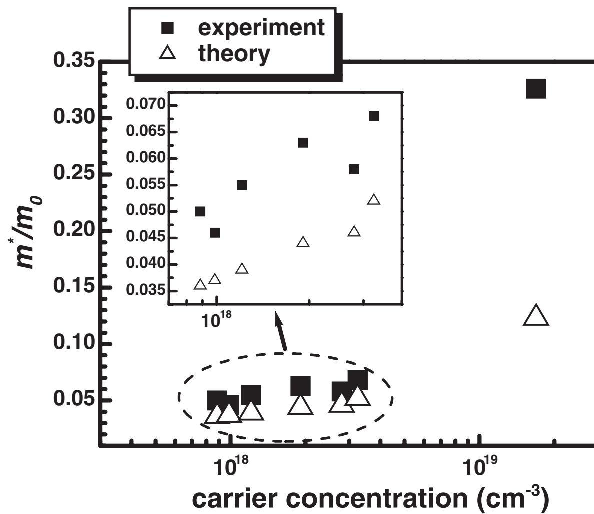

Fig. 13. Electron effective mass versus residual carrier concentration from the present experimental data for $InAs_{1-x}N_x$ samples with different nitrogen compositions. The open triangles are the theoretically calculated mass. The inset shows the magnified part of the region marked by the dotted circle.

the BAC model that predicts an enhancement in the electron effective mass of the III–V–N alloys. The discrepancy between the calculated and the experimental data might be due to (i) the nonparabolicity effect in the degenerate semiconductors. Since in our samples the Fermi level E_F is located at least 90 meV above the conduction band minimum, one should take into account the contribution of the nonparabolicity effect to the value of m^* and the effect is expected to be more pronounced in this small band-gap energy InAsN material. It may cause an increase of the effective mass with respect to m^* at the bottom of the conduction band [m^* (0)]. (ii) Nitrogen-induced Γ–L–X intermixing on the conduction band edge.[9,43] The X and L electrons of InAs have heavier mass than the Γ conduction band edge of InAs. However, the exact reason for the discrepancy is still not clear and is under further investigation.

4. Conclusions

In summary, the structural, electrical, and optical properties of bulk InAsN alloys grown using GSMBE were investigated. When N composition increases, InAsN film has broader linewidth in the DXRD spectrum and higher residual carrier concentration. The possible origin of the high residual carrier concentration in N-containing sample is not quite clear so far. However, due to the Burstein–Moss effect resulting from the residual carrier concentration, the absorption edge of InAsN alloy, as compared to that of InAs, shows a blue shift. To deduce the 'real' band-gap energy of our InAsN samples, the energy shift due to the Burstein–Moss effect and the band-gap narrowing effect are calculated using a self-consistent approach based on the band-anticrossing model. After the correction, the bowing effect reappears in these InAsN samples. In addition, from the infrared reflectivity and Hall-effect measurements of these degenerate InAsN samples, we found a sizeable increase of the electron effective mass in these InAsN alloys, which is consistent with the theoretical results predicted by the band-anticrossing model.

Acknowledgements

This work was supported by the National Science Council and the Ministry of Education of the Republic of China under Contract nos. NSC 89-2215-E-002-034 and 89-N-FA01-2-4-3, respectively.

1) M. Kondow, K. Uomi, T. Kitatani, S. Watahiki and Y. Yazawa: J. Cryst. Growth **164** (1996) 175.
2) M. Kondow, T. Kitatani, S. Nakatsuka, M. C. Larson, K. Nakahara, Y. Yazawa, M. Okai and K. Uomi: IEEE J. Sel. Top. Quantum Electron. **3** (1997) 719.
3) W. G. Bi and C. W. Tu: Appl. Phys. Lett. **72** (1998) 1161.
4) S. Sakai, Y. Ueta and Y. Teauchi: Jpn. J. Appl. Phys. **32** (1993) 4413.
5) S. H. Wei and A. Zunger: Phys. Rev. Lett. **76** (1996) 664.
6) L. Bellaiche, S. H. Wei and A. Zunger: Phys. Rev. B **54** (1996) 17568.
7) J. Neugebauer and C. G. Van de Walle: Phys. Rev. B **51** (1995) 10568.
8) A. Rubio and M. L. Cohen: Phys. Rev. B **51** (1995) 4343.
9) T. Mattila, S.-H. Wei and A. Zunger: Phys. Rev. B **60** (1999) R11245.
10) W. Shan, W. Walukiewicz, J. W. Ager III, E. E. Haller, J. F. Geisz, D. J. Friedman, J. M. Olson and S. R. Kurtz: Phys. Rev. Lett. **82** (1999) 1221.
11) W. Shan, W. Walukiewicz, K. M. Yu, J. W. Ager III, E. E. Haller, J. F. Geisz, D. J. Friedman, J. M. Olson, S. R. Kurtz, H. P. Xin and C. W. Tu: Phys. Status Solidi B **223** (2001) 75.
12) J. S. Wang, H. H. Lin and L. W. Sung: IEEE J. Quantum Electron. **34** (1998) 1959.
13) D. K. Shih, H. H. Lin and Y. H. Lin: Electron. Lett. **37** (2001) 1342.
14) E. Burstein: Phys. Rev. **93** (1954) 632.
15) D. K. Shih, H. H. Lin, L. W. Song, T. Y. Chu and T. R. Yang: Proc. 13th Int. Conf. Indium Phosphide and Related Materials, Nara, Japan, May 2001, IEEE, Piscatauay, NJ, 2001 p. 555.
16) J. W. Matthews and A. E. Blakeslee: J. Cryst. Growth **27** (1974) 118.
17) V. Swaminathan and A. T. Macrander: *Materials Aspects of GaAs and InP Based Structures* (Prentice-Hall, New Jersey, 1991) Chap. 1.
18) C. Skierbiszewski, P. Perlin, P. Wisniewski, W. Knap, T. Suski, W. Walukiewicz, W. Shan, K. M. Yu, J. W. Ager, E. E. Haller, J. F. Geisz and J. M. Olson: Appl. Phys. Lett. **76** (2000) 2409.
19) C. Skierbiszewski, P. Perlin, P. Wisniewski, T. Suski, W. Walukiewicz, W. Shan, J. W. Ager, E. E. Haller, J. F. Geisz, D. J. Friedman, J. M. Olson and S. R. Kurtz: Phys. Status Solidi B **216** (1999) 135.
20) Y. Makita, H. Ijuin and S. Gonda: Appl. Phys. Lett. **28** (1976) 287.
21) H. P. Hjalmarson, P. Vogl, D. J. Wolford and J. D. Dow: Phys. Rev. Lett. **44** (1980) 810.
22) Y. C. Ruan and W. Y. Ching: J. Appl. Phys. **62** (1987) 2885.
23) J. Stiens and R. Vounckx: J. Appl. Phys. **76** (1994) 3526.
24) A. Lindsay and E. P. O'Reilly: Solid State Commun. **112** (1999) 443.
25) W. Shan, W. Walukiewicz, J. W. Ager III, E. E. Haller, J. F. Geisz, D. J. Friedman, J. M. Olson and S. R. Kurtz: J. Appl. Phys. **86** (1999) 2349.
26) L. Bellaiche, S. H. Wei and A. Zunger: Phys. Rev. B **56** (1997) 10233.
27) W. Dobbelaere, J. De Boeck, P. Van Mieghem, R. Mertens and G. Borghs: J. Appl. Phys. **69** (1991) 2536.
28) I. H. Lee, J. J. Lee, P. Kung, F. J. Sanchez and M. Razeghi: Appl. Phys. Lett. **74** (1999) 102.
29) X. Zhang, S. J. Chua, W. Liu and K. B. Chong: Appl. Phys. Lett. **72** (1998) 1890.
30) D. C. Reynolds, D. C. Look and B. Jogai: J. Appl. Phys. **88** (2000) 5760.
31) I. Suemune, K. Uesugi and W. Walukiewicz: Appl. Phys. Lett. **77** (2000) 3021.
32) P. J. Klar, H. Grüning, W. Heimbrodt, J. Koch, F. Höhnsdorf, W. Stolz, P. M. A. Vicente and J. Camassel: Appl. Phys. Lett. **76** (2000) 3439.
33) K. M. Yu, W. Walukiewicz, J. Wu, J. W. Beeman, J. W. Ager III, E. E. Haller, W. Shan, H. P. Xin and C. W. Tu: Appl. Phys. Lett. **78** (2001) 1077.
34) H. Naoi, Y. Naoi and S. Sakai: Solid-State Electron. **41** (1997) 319.
35) T. Yang, S. Nakajima and S. Sakai: Jpn. J. Appl. Phys. **36** (1997) L320.

36) J. S. Wang, H. H. Lin, L. W. Song and G. R. Chen: J. Vac. Sci. Technol. B **19** (2001) 202.
37) H. Saito, T. Makimoto and N. Kobayashi: J. Cryst. Growth **195** (1998) 416.
38) S. Francoeur, G. Sivaraman, Y. Qiu, S. Nikishin and H. Temkin: Appl. Phys. Lett. **72** (1998) 1857.
39) L. Bellaiche and A. Zunger: Phys. Rev. B **57** (1997) 4425.
40) P. N. Hai, W. M. Chen, I. A. Buyanova, H. P. Xin and C. W. Tu: Appl. Phys. Lett. **77** (2000) 1843.
41) P. Perlin, E. Litwin-Staszewska, B. Suchanek, W. Knap, J. Camassel, T. Suski, R. Piotrzkowski, I. Grzegory, S. Porowski, E. Kaminska and J. C. Chervin: Appl. Phys. Lett. **68** (1996) 1114.
42) P. Y. Yu and M. Cardona: *Fundamentals of Semiconductors: Physics and Materials Properties* (Springer-Verlag, Berlin, Heidelberg, 1996) Chap. 6.
43) A. Zunger: Phys. Status Solidi B **216** (1999) 117.